Journal of *Marine Science and Engineering*

MDPI

Article

Numerical Simulation of Tidal Flow Around Offshore Wind Turbine Monopile Array Using a Structural Drag Source-Term Approach

Fangyu Wang [1,2], Dongfang Liang [2], Jisheng Zhang [1,*], Yakun Guo [3] and Hao Chen [1]

[1] College of Harbor, Coastal and Offshore Engineering, Hohai University, Nanjing 210024, China; fywang@hhu.edu.cn (F.W.); chenhao2151@126.com (H.C.)
[2] Department of Engineering, University of Cambridge, Cambridge CB2 1PZ, UK; dl359@cam.ac.uk
[3] Faculty of Management, Sciences & Engineering, University of Bradford, Bradford BD7 1DP, UK; y.guo16@bradford.ac.uk
* Correspondence: jszhang@hhu.edu.cn

Abstract

The increasing deployment of dense offshore wind turbine monopile foundations pose significant challenges for accurately simulating tidal-flow modification and energy transport at the array scale. Balancing physical realism with computational efficiency remains a key challenge in hydrodynamic modelling of offshore wind farms. In this study, an established drag-based source-term approach is implemented through a dedicated module developed within the TELEMAC-3D framework to represent the momentum-blocking effects of offshore wind-farm arrays. A representative dense 8 × 10 wind turbine monopile array configuration is constructed in a typical tidal channel to systematically examine array-induced tidal-flow responses. The results indicate that the drag-based source-term approach preserves the regional-scale tidal flow structure while effectively capturing array-induced local velocity adjustments and pronounced downstream wake attenuation and recovery. Detailed analyses further reveal distinct spatial and temporal characteristics of the velocity response, including the decay and recovery of velocity deviations downstream of the array. In addition, the monopile array induces a clear modulation of flow kinetic energy, characterized by enhanced energy dissipation and a finite array-scale redistribution of kinetic energy. These findings demonstrate that this approach efficiently simulates the array-scale hydrodynamic and energetic impacts of large offshore wind farms and contribute to a better understanding of array-induced tidal flow modification and energy redistribution.

Keywords: wind turbine monopile array; TELEMAC-3D; structural drag source-term; tidal current

Check for updates

Academic Editors: Magda Catarina Sousa, Ana Picado and Carina Lurdes Lopes

Received: 22 March 2026
Revised: 16 April 2026
Accepted: 21 April 2026
Published: 22 April 2026

Copyright: © 2026 by the authors. Licensee MDPI, Basel, Switzerland. This article is an open access article distributed under the terms and conditions of the Creative Commons Attribution (CC BY) license.

1. Introduction

Offshore wind energy is a key component of the global transition toward low-carbon energy systems [1]. As installed capacity continues to expand and turbine ratings increase, wind-farm foundations are increasingly deployed in dense configurations within nearshore and shallow-water regions. Such large-scale structural array can substantially modify local hydrodynamic conditions, influencing tidal-current distribution, energy transfer, and seabed processes [2,3]. Previous studies have shown that flow-structure interactions induce momentum dissipation and flow filed redistribution, which in turn alter tidal-current

energy availability and bed-shear-stress patterns [4]. Accurately representing these array-induced effects while retaining computational efficiency remains a central challenge for regional-scale modelling of offshore wind farms.

Laboratory studies have provided substantial insight into the near-field flow characteristics of isolated piles and small array, including flow separation, vortex shedding, and local scour dynamics [5–7]. However, these studies elucidate the fundamental physics of flow-pile interaction but are difficult to extrapolate to array-scale assessments, where device spacing, wake merging, and large-scale momentum budgets play dominant roles [8]. As a result, numerical modelling has become an essential tool for investigating hydrodynamic impacts at the scale of offshore wind-farm array.

With advances in computational capability, three-dimensional hydrodynamic models have become essential for studying flow modification induced by multiple arrays [9]. A key challenge lies in accurately parameterizing the structural effects of monopile foundations when transferring near-field insights into regional-scale numerical models, as these representations strongly influence model performance. To balance physical fidelity and computational cost, several structural representation strategies have been developed. The bottom-friction parameterization represents the additional momentum dissipation induced by turbine array through adjusting the bed-friction coefficient. It assumes that the presence of piles can be equivalently expressed as an enhancement of local bed friction, reflecting the array's averaged drag effect on the flow filed [10]. This approach is computationally efficient and suitable for preliminary or regional-scale simulations. However, as a bulk parameterization, it has limited capability to solve local velocity deficits, wake structures around individual piles, or momentum redistribution within the array [11]. The geometric mask method treats foundations as solid obstacles within the computational domain. By masking the regions occupied by the piles, the flow velocity inside them is forced to zero, preventing fluid from passing through the pile locations. This method (i.e., hole-cutting) explicitly reproduces the geometric obstruction of the structures and can capture flow separation, reattachment, and wake structures around them [12]. While capable of capturing flow separation and near-wake vortices [6,13], it requires high-resolution meshing, making it prohibitively expensive for large-scale simulation [14]. Among these approaches, drag-based source-term methods provide a promising balance between computational efficiency and physical representation, making them particularly suitable for large-scale simulations of dense turbine array. Therefore, recent research has increasingly focused on the development and refinement of drag-based formulations. The method introduces a body-force term proportional to the square of the flow velocity into the momentum equations, thereby parameterizing the momentum dissipation induced by the structures. The array-induced drag effects can be represented continuously without altering the mesh topology [15,16]. Its theoretical basis lies in representing the cumulative momentum loss induced by multiple structures through a continuously distributed volumetric drag formulation. Vennell [17] further analyzed the energy conversion efficiency under varying array densities and channel-scale conditions. Building upon this concept, Funke et al. [18] implemented this approach numerically and proposed a distributed drag modeling framework based on momentum kernel functions. Subsequent improvements were introduced by Coles et al. [19], who verified the applicability of the volumetric drag source term in reproducing array-scale velocity reduction and flow field redistribution. Kramer and Piggott [20] examined the consistency of drag-based parameterizations in shallow-water models and proposed corrections to the enhanced bottom-drag formulation, highlighting the importance of physically consistent drag source terms when representing turbine-induced momentum loss in regional-scale simulations. At the regional scale, the sensitivity of modelled flow response to source-term parameters was systematically investigated.

Rivier et al. [21] conducted a systematic regional-scale evaluation of the influence of source-term parameters on flux distribution. Their results demonstrated that this approach can effectively reproduce observed flow-structure variations while maintaining overall momentum conservation. With the advancement of research, drag-based source-term approach has been progressively refined and synthesized, with recent reviews highlighting their improved numerical robustness and scalability for representing multiple foundations array in hydrodynamic models [22]. Beyond tidal turbine array, the same drag-based source-term formulation has recently been extended to represent resistance effects in other distributed structures [23]. In summary, the evolution of this approach can be seen as three phases: theoretical foundation, numerical implementation and validation in idealized channels, and recent methodological syntheses.

Despite these advances, several key challenges remain. First, although drag-based source-term method has been widely applied in the context of tidal stream turbine array or other distributed structures, their application to offshore wind-farm array remains comparatively limited. Second, existing studies of offshore wind-farm array predominantly rely on the geometric mask method or bottom-friction parameterization, which can be computationally demanding when extended to large-scale simulations. In contrast, drag-based formulations offer a computationally efficient and scalable alternative, yet their applicability to offshore wind-farm array under regional-scale conditions remains less systematically explored. To address these gaps, this study implements an established drag-based source-term approach within the TELEMAC-3D model to represent the momentum-blocking effects of offshore wind-farm array. The primary objective is to evaluate the applicability and performance of this approach for regional-scale hydrodynamic assessment, with a focus on its ability to reproduce tidal current modification and flow field redistribution.

The work is organized as follows: Section 2 describes the numerical models, and Section 3 presents the model setup and validation. Section 4 then presents the results and discussion, which is divided into three parts. Section 4.1 examines the overall flow response to the wind farm, including general flow field characteristics and array-scale wake structures. Section 4.2 focuses on the array-induced velocity response, covering the spatial distribution, decay/recovery, and temporal response of velocity deviations. Section 4.3 discusses the array-induced modulation of flow kinetic energy, analyzing the spatial distribution and radial extent of the array effects. Finally, Section 5 presents the main conclusions of this study.

2. Numerical Models

TELEMAC [24] is an open-source numerical system for simulating free-surface hydrodynamics, which includes TELEMAC-2D, TELEMAC-3D, etc. The model utilizes unstructured and dynamically adaptable meshes to accurately represent complex terrains, with local mesh refinement in areas of interest. Using a finite element discretization scheme, it incorporates multiple turbulence models and robust iterative solvers to resolve the vertical structure of the hydrodynamic field [25].

2.1. TELEMAC-3D

2.1.1. Governing Equations

In the tidal current simulation, the TELEMAC-3D module (V8p4r0 version) is governed by the non-hydrostatic Navier–Stokes equations and the continuity equation. In the vertical direction, a σ-coordinate transformation is adopted, in which σ varies from 0 at the seabed to 1 at the free water surface. Assuming the fluid is incompressible [26], the effects of

temperature and salinity are neglected in the simulation. The governing equations in the Cartesian coordinates are as follows:

$$\frac{\partial U}{\partial x} + \frac{\partial V}{\partial y} + \frac{\partial V}{\partial z} = 0 \tag{1}$$

$$\frac{\partial U}{\partial t} + U\frac{\partial U}{\partial x} + V\frac{\partial U}{\partial y} + W\frac{\partial U}{\partial z} = -\frac{1}{\rho_{water}}\frac{\partial P_{pre}}{\partial x} + v\Delta(U) + F_x \tag{2}$$

$$\frac{\partial U}{\partial t} + U\frac{\partial U}{\partial x} + V\frac{\partial U}{\partial y} + W\frac{\partial U}{\partial z} = -\frac{1}{\rho_{water}}\frac{\partial P_{pre}}{\partial y} + v\Delta(V) + F_y \tag{3}$$

$$\frac{\partial U}{\partial t} + U\frac{\partial U}{\partial x} + V\frac{\partial U}{\partial y} + W\frac{\partial U}{\partial z} = -\frac{1}{\rho_{water}}\frac{\partial P_{pre}}{\partial z} + v\Delta(W) + F_z \tag{4}$$

where U, V, and W are the velocity components in the x, y, and z directions, respectively; F_x, F_y, and F_z represent the source terms of the fluid in the x, y, and z directions, respectively; Δ denotes the three-dimensional Laplacian operator; ρ_{water} is water density; t is the time; v is the kinematic viscosity ($v = 1 \times 10^{-6}$ m^2/s); P_{pre} is the total pressure, which is the sum of the atmospheric pressure on the water surface (P_{atm}) and the hydrostatic pressure (P_d) and can be calculated as follows:

$$P_{pre} = P_{atm} + \rho_{water} g(z_s - z) + P_d \tag{5}$$

where z_s represents the free surface elevation.

In this study, the source terms include a structural drag source term used to represent the momentum-blocking effects of monopiles, which is described in detail in Section 2.2. The governing equations are solved using a semi-implicit numerical scheme.

2.1.2. Initial Conditions

The initial velocity field is initialized using the mapped velocity field derived from the TOPEX/Poseidon global tidal model (TPXO, TPXO10-atlas-v2 version), based on the Laplace tidal equations and satellite altimetry observations processed using the OSU Tidal Prediction Software [27]. The simulation focuses on barotropic tidal currents, and density stratification effects are neglected, while the Coriolis force is included in the momentum equations. To minimize the influence of initial transients, a spin-up period was applied [28]. Given that the TPXO forcing includes multiple tidal constituents, the shortest periods are semidiurnal. Accordingly, the 3–4-day spin-up corresponds to approximately 6–8 semidiurnal tidal cycles, which ensures that the flow field reaches a quasi-periodic state. Therefore, a 4-day spin-up was used for validation tests to provide a conservative margin, while 3 days were deemed sufficient for scenario simulations. The initial free-surface elevation is set to zero, and the model is allowed to adjust dynamically during the spin-up period.

2.1.3. Boundary Conditions

The global tidal model TPXO provides the tidal forcing at the open-sea boundary and is among the most accurate available [29]. It includes 13 tidal constituents: M2, S2, N2, K2, K1, O1, P1, Q1, M4, Ms4, Mn4, Mm, and Mf, on a 1/6° spatial resolution grid. The land boundary is treated as a closed boundary, where both water and velocity fluxes are set to zero. During the simulation, the water level and horizontal velocity components (U and V) at the open boundary are expressed as the sum of harmonic constituents that vary over time and space. For each constituent, the water level or velocity component can be calculated as follows:

$$f(x, y, t) = \sum_i f_i(x, y, t) \tag{6}$$

$$f_i(x,y,t) = f_i(t)A_{f_i}(x,y)\cos\left(2\pi\frac{t}{T_i} - \beta_{f_i}(x,y) + \beta_i^0 + g_i(t)\right) \quad (7)$$

where f denotes either the water depth or one component of the horizontal velocity (U or V); i is the index of the tidal constituent; T_i is the period of harmonic components; A_{fi} and β_{fi} are the amplitude and phase of variable f for the i-th constituent, respectively, while β_{0i} denotes the initial phase. The functions $f_i(t)$ and $g_i(t)$ represent the nodal factors that account for the lunar modulation of tidal effects. Both A_{fi} and β_{fi} depend solely on spatial location and remain constant in time.

In addition to the tidal boundary forcing described above, bottom friction is parameterized using a quadratic friction law to represent near-bed momentum dissipation. The structural drag is vertically distributed to represent the depth-integrated momentum loss induced by monopiles.

2.2. Principle and Implementation

To characterize the influence of wind turbine foundation array (monopiles) on the momentum distribution of tidal currents, a structural drag source term was introduced into the TELEMAC-3D model. This source term adds body forces to the momentum equations to represent the resistance effect of monopiles on the surrounding flow. It should be noted that this source term represents flow resistance and momentum dissipation, not energy conversion or extraction. The time step, kernel radius, and drag coefficient are selected to satisfy numerical stability constraints associated with the explicit treatment of the momentum source term.

2.2.1. Theoretical Formulation

In offshore wind farms, strong interactions occur between wind turbine monopiles and the surrounding flow, resulting in local momentum dissipation and flow field redistribution. For large-scale numerical models, directly resolving the detailed flow around each pile is computationally prohibitive. Therefore, a parameterized drag source term is introduced to represent the drag effect of monopiles as a continuous body force distributed over the control volume, allowing the averaged resistance effect to be captured at the macro scale. This source term follows the classical drag force formulation for bluff bodies [30,31], and the structural drag force term can be expressed as

$$F_D = -\frac{1}{2}\rho_{water}C_D A_{ref} U_{in}|U_{in}| \quad (8)$$

where C_D is the structural drag coefficient, A_{ref} is a reference area representing the projected area of the pile at a characteristic scale, and the source term acts opposite to the local flow velocity U_{in}, representing the momentum loss induced by the pile. $|U_{in}|$ denotes the magnitude of the local flow velocity vector U_{in}.

If the body force is applied only at a single grid point, it may cause numerical instability and unrealistic local momentum losses. To avoid this, a spatial smoothing kernel is introduced to distribute the drag effect continuously around the pile, forming an effective drag cloud in the computational domain. The kernel radius typically ranges from several times the pile diameter to several grid spacings, depending on the local resolution and numerical stability. The kernel function generally takes the following form:

$$W(r) = exp\left[-\left(\frac{r}{R_{kernel}}\right)^2\right] \quad (9)$$

where r denotes the horizontal distance from the pile center, and R_{kernel} defines the spatial decay range of the drag field.

To ensure conservation of total momentum dissipation in the numerical sense, the kernel function is normalized as shown in Equation (10):

$$\int_{V_d} W(r) dV_{ol} = 1 \tag{10}$$

where V_{ol} denotes the control volume over which the kernel function is integrated, V_d is the drag distribution volume.

For the overall effect of a monopile array, structural drag is represented as a volumetrically distributed drag force source term constructed from kernel functions, thereby capturing the cumulative effect of the array at the model scale.

2.2.2. Implementation Method

A self-implemented structural drag source-term module, following the approach of [18], is implemented within the TELEMAC-3D framework as a dynamically evaluated drag force source term. In the numerical implementation, the structural drag is introduced as an additional source term in the momentum equations. It is treated explicitly within the semi-implicit hydrodynamic solver of TELEMAC-3D, with the source term evaluated dynamically at each time step.

For each horizontal grid node, the horizontal distance to the center of each monopile is computed. A Gaussian-based kernel is adopted to enhance numerical robustness in the near-pile region. To account for non-uniform mesh geometry, the kernel weights are area-weighted and subsequently normalized, ensuring conservation of the total applied drag force over the horizontal mesh. For each monopile, the drag force is evaluated based on a representative inflow velocity, computed as a horizontally weighted spatial average of the surrounding flow within a prescribed neighborhood around the pile center. This representative velocity is then distributed across the vertical layers in proportion to the local layer thickness, ensuring consistency with the depth-integrated representation of the pile-induced drag. The resulting drag force associated with each pile is distributed to the surrounding mesh nodes according to the corresponding kernel weights. The kernel radius R_{kernel} is prescribed as a model parameter and determines the spatial extent over which the pile-induced drag is applied.

In the present simulations, the kernel radius is set equal to the monopile diameter, which controls the spatial extent of the applied drag force and ensures numerical robustness of the explicit source-term treatment. Additionally, kernel support is truncated beyond a prescribed cutoff distance for computational efficiency. At each horizontal grid point, the total structural drag is obtained by accumulating the contributions from all piles whose kernel support overlaps the local mesh, thereby representing array-scale momentum dissipation in a spatially distributed and dynamically coupled manner.

2.2.3. Coupling with the Hydrodynamic Solver

Within the three-dimensional hydrodynamic framework, the structural drag source term is coupled directly to the momentum equations of TELEMAC-3D. After being constructed on the horizontal plane, the drag source term is vertically distributed uniformly throughout the water depth. This treatment ensures that the depth-integrated drag force remains consistent with the pile-based parameterization while allowing the pile-induced resistance to be projected into the full three-dimensional domain.

In the discrete form, the horizontal components of the structural drag source term can be written as Equation (11):

$$S_{x,y} = -\frac{1}{2}\rho_{water} C_D \left(\frac{D_{pile}}{A_{kern}}\right) U_{in}|U_{in}| W(r) \tag{11}$$

where D_{pile} is the pile diameter, and A_{kern} represents the integrated area of the truncated Gaussian kernel within its influence radius.

The drag source term is applied consistently with the model time-stepping procedure without altering the original structure of the hydrodynamic solver. By directly incorporating directionally resolved drag forces into the three-dimensional momentum equations, this coupling strategy enables accurate reproduction of the modulation effects of the monopile array on tidal momentum and flow field distribution, without explicitly resolving local pile-scale flow structures.

3. Model Set-Up and Validation

3.1. Model Set-Up

3.1.1. Study Area

The nearshore region off the northern Shandong Peninsula, China, was selected as the numerical simulation domain (Figure 1). This region lies at the junction of the Yellow Sea and the Bohai Sea, with geographical coordinates of approximately 120° E–123° E and 36.0° N–38.5° N. Influenced by the peninsula's complex topography, the coastline is highly indented, forming diverse local hydrodynamic patterns. The nearshore water depth is generally less than 10 m and gradually increases to about 70 m offshore, with isobaths extending seaward in a fan–shaped pattern. The region is characterized by a regular semidiurnal tide, driven by the combined influence of the East Asian monsoon and the tidal regime. As a representative shallow coastal area in the northern Yellow Sea, this region is characterized by strong tidal currents and increasing offshore wind energy development, making it particularly suitable for investigating monopile array-induced hydrodynamic modifications at both local and regional scales.

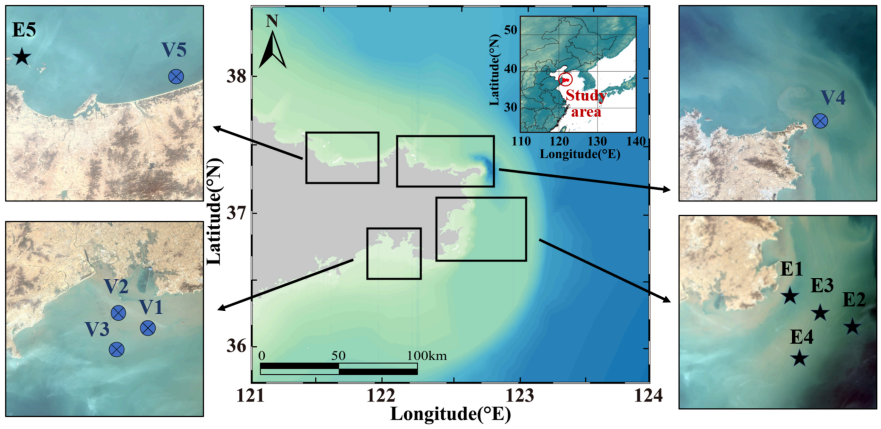


Figure 1. Location of the study area and the observation stations.

3.1.2. Mesh Generation and Sensitivity Analysis

To achieve a reasonable balance between computational accuracy and efficiency, a grid sensitivity analysis was conducted to determine the appropriate horizontal resolution. The computational domain was discretized using an unstructured triangular mesh to accommodate the complex shoreline geometry and variations in bathymetric gradients. To better resolve the hydrodynamic interactions around the array, a local mesh refinement was applied in the offshore area. Except for the horizontal grid resolution, all other model settings were kept identical throughout the sensitivity tests, including the time step, vertical layering, and boundary conditions, with only the horizontal mesh scale being varied. A vertical resolution was selected based on previous regional tidal modelling studies in similar shallow-water environments, providing a reasonable compromise between resolving vertical shear and computational efficiency.

As shown in Table 1, four candidate grids (G1–G4) were constructed with progressively refined resolutions to systematically evaluate the influence of horizontal resolution on the simulation results. The sensitivity analysis indicates that the resolutions of G1 and G2 were relatively coarse, leading to larger deviations between the simulated and observed tidal elevations and current velocities. With increasing resolution, the deviations gradually decreased and became nearly convergent between G3 and G4. The differences in the main evaluation metrics between these two grids were small, and the spatial distribution patterns of tidal currents were also largely consistent. However, the computational cost of G4 increased significantly, with the number of mesh elements being approximately 3.17 times that of G3, and the total computation time about 4.7 times longer, while the improvement in accuracy was relatively limited.

Table 1. Grid sensitivity analysis of the numerical model.

Grid List	Number of Grid of Nodes	Number of Elements	Min. Size (m)	Max. Size (m)	Growth Rate	Vertical Layers
1	47,589	98,102	150	800	1.30	6
2	161,616	321,195	80	800	1.17	6
3	459,376	917,909	5	1400	1.10	6
4	1,120,429	2,439,097	5	1400	1.02	6

Considering both computational accuracy and efficiency, grid G3 was finally selected as the unified mesh for all subsequent simulations. This grid provides a good representation of shorelines, bays, and bathymetric gradients, achieving a balance between model accuracy and computational cost, and ensuring the comparability of results among different physical scenarios.

3.1.3. Initial and Boundary Conditions

The open boundary was located in the central Yellow Sea, where tidal forcing was driven by the main harmonic constituents provided by the TPXO global tidal database. The initial water level was obtained from the superposition of harmonic components, while the initial velocity field was set to zero. The land boundaries were specified as impermeable (no-flow) conditions. Bottom friction was parameterized based on the median sediment size, with the Nikuradse roughness height defined as Equation (12):

$$k_s = 2.5 d_{50} \tag{12}$$

where d_{50} is the median sediment grain size.

The model used a σ-coordinate system with six vertical layers, and the time step of 10 s satisfied the CFL stability criterion. All subsequent simulations were conducted on the G3 mesh to ensure consistency and comparability among different scenarios.

3.2. Model Validation

3.2.1. Tidal Validation in the Prototype Domain

To ensure the accuracy of the tidal model, data from five tidal elevation stations, three depth-averaged velocity stations, and two vertically stratified velocity stations are used for model validation. Figure 1 and Table 2 show the details of these measurements.

Figure 2 compares the observed tidal elevations with the simulated results at five tidal stations (E1–E5). Stations E1–E4 include both summer (orange squares) and winter (blue circles) measurements, allowing assessment of the model's seasonal performance under varying hydrodynamic conditions. Station E5, although not separated by season, spans

a relatively long observation period (green triangles), providing additional validation of the model's long-term stability. Overall, the simulated tidal elevations are in reasonable agreement with the observations. The model captures both the phase and amplitude of the dominant tidal constituents well, with only minor discrepancies at certain peaks and troughs, indicating satisfactory overall accuracy of the tidal-elevation simulation.

Table 2. Observation station.

Hydrodynamic	Station	Time
Tidal elevation	E1 E2 E3 E4	19 August 2017–27 August 2017 24 February 2018–02 March 2018
	E5	07 May 2015–20 May 2015
Tidal velocity	V1 V2 V3	20 November 2010–23 November 2010; 29 November 2010–31 November 2010
	V4	10 July 2009–16 July 2009
	V5	21 May 2015–22 May 2015

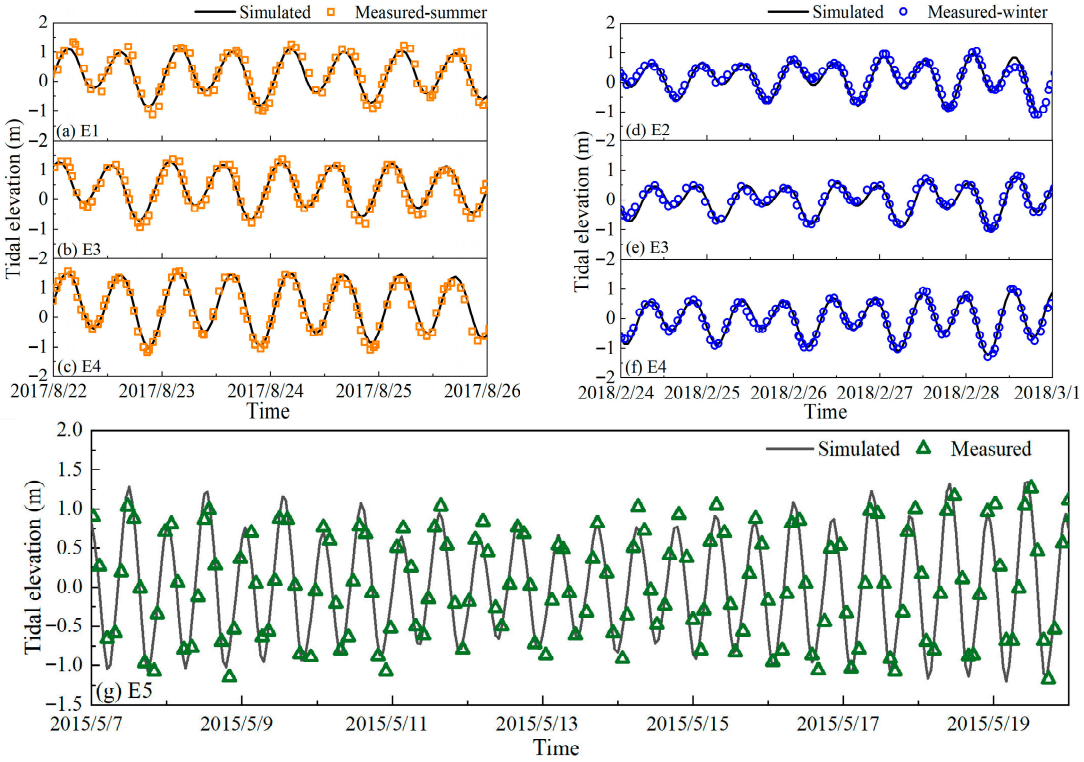


Figure 2. Comparison between simulated (solid lines) and measured (symbols) tidal elevations at five stations: (**a**–**c**) E1, E3, E4 in summer; (**d**–**f**) E2, E3, E4 in winter; and (**g**) E5 for a long-term observation period.

Figure 3 compares the simulated and measured tidal velocity and direction at the three observation stations (V1–V3). The model reproduces the temporal variations of tidal currents in good agreement with the field measurements. At all stations, the simulated velocity aligns with the observed data in both magnitude and phase, and the ebb-flood cycles are accurately represented under spring and neap tidal conditions. The simulated current directions also capture the observed rotational and reversal patterns throughout

each tidal cycle, indicating that the model can effectively describe the periodic variations in flow orientation. Minor discrepancies occur near several turning points or extreme values, likely due to local bathymetric influences or measurement uncertainties. Overall, the results confirm that the model provides a reliable representation of the tidal current dynamics in the study area.

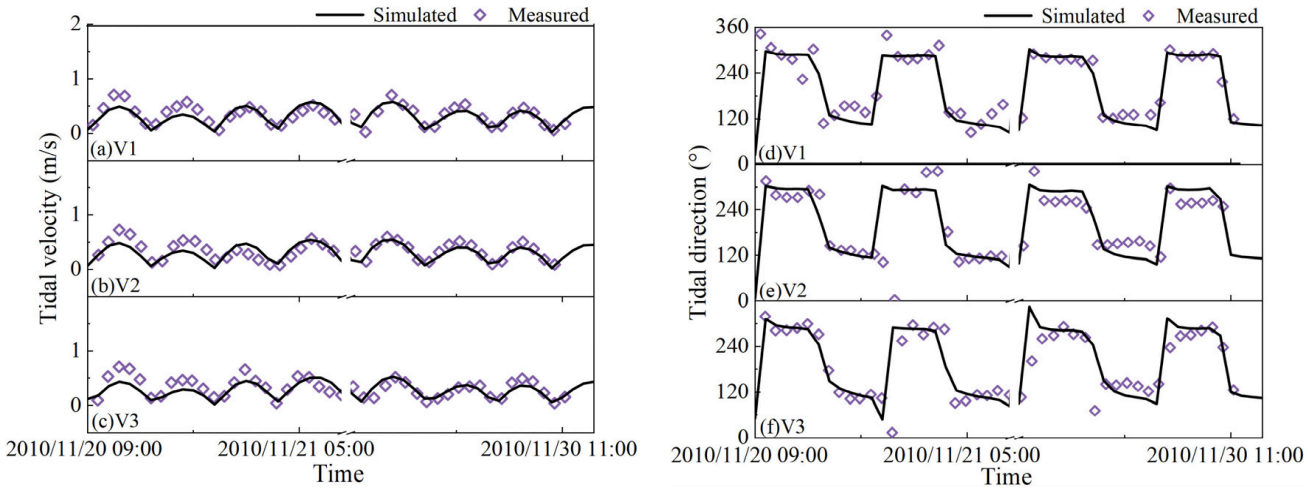


Figure 3. Comparison between simulated (solid lines) and measured (symbols) tidal velocity and direction at the V1, V2, and V3 stations: (**a**–**c**) tidal velocity and (**d**–**f**) tidal direction.

Furthermore, Figures 4 and 5 compare the simulated and measured tidal velocity and direction at three vertical layers in the water column at Stations V4 and V5. The model captures the main vertical and temporal variations of tidal currents, with simulated amplitudes and phases closely matching the field observations. The periodic reversals of current direction are also captured, indicating that the model can reasonably describe the three-dimensional tidal dynamics. Minor discrepancies remain, mainly manifested as slight underestimation near the bottom at V4 and weaker surface currents with small phase lags at V5, which are likely related to near-bed friction and surface turbulence. Nevertheless, these deviations are minor and do not affect the overall agreement, confirming that the model can reasonably simulate the three-dimensional tidal dynamics in the study area.

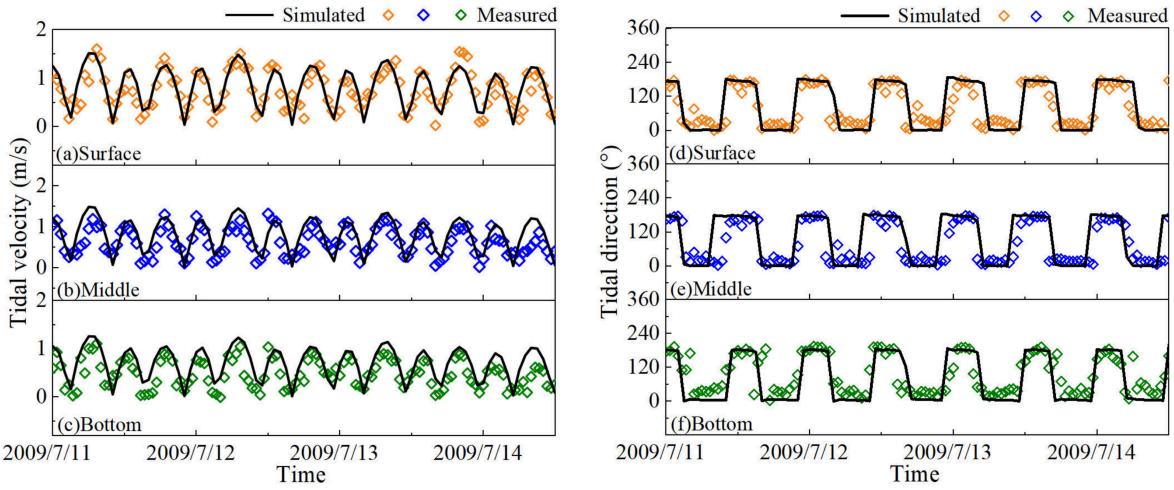


Figure 4. Comparison between simulated and measured tidal velocity and direction at three vertical layers in the water column at station V4: (**a**,**d**) surface, (**b**,**e**) middle depth, and (**c**,**f**) bottom.

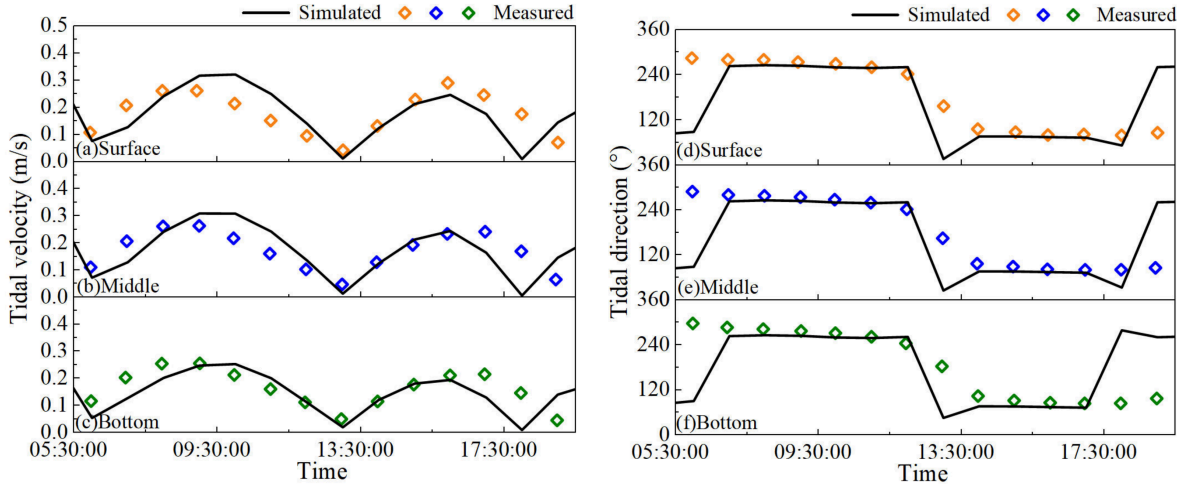


Figure 5. Comparison between simulated and measured tidal velocity and direction at three vertical layers in the water column at station V5: (**a**,**d**) surface, (**b**,**e**) middle depth, and (**c**,**f**) bottom.

In summary, the validation results confirm that the model can adequately capture the regional tidal regime and resolve the vertical structure of tidal currents, ensuring a robust hydrodynamic framework for subsequent analyses.

3.2.2. Structural Drag Approach Validation (Monopile Test)

To validate the applicability of the structural drag source-term approach at the monopile scale, an idealized monopile test was conducted following the experimental conditions reported by Roulund et al. [6]. The computational domain was configured as a rectangular flume with a length of 35 m, a width of 3 m, and a uniform water depth of 0.54 m. A constant inflow velocity of U_0 = 0.326 m/s was prescribed, and the monopile diameter was set to D = 0.536 m. The monopile was represented by an equivalent body force applied at the pile center, enabling an assessment of the model's capability to reproduce wake characteristics and associated momentum dissipation.

Figure 6 shows that the implemented drag source-term method captures the primary hydrodynamic features induced by a monopile at mid- to upper-water depths. Upstream of the monopile, the model shows the continuous deceleration of the incoming flow resulting from monopile blockage, with streamwise velocity variations in good agreement with experimental measurements. However, when the measurement location approaches the bed (z < 0.02 m), the agreement between simulated and measured velocities upstream of the monopile deteriorates. In the downstream region, discrepancies are also evident in the near-wake zone. While the experiments exhibit pronounced flow recirculation and strong vortex structures, the present simulations yield a comparatively smoother representation of these local flow features. The agreement between the model and reference data is further quantified using the mean absolute error (MAE), as summarized in Table 3. It should be noted that the MAE is computed using the experimental data of Roulund et al. [6] as the reference and the numerical results as the predictions.

Table 3. Mean Absolute Error (MAE, unit: m/s) between the numerical results (present drag source-term model and geo-mask model) and the experimental data of Roulund et al. [6].

Grid List	Z = 0.2	Z = 0.1	Z = 0.05	Z = 0.02	Z = 0.01	Z = 0.005
This study	0.0238	0.0496	0.0649	0.110	0.129	0.139
Geo mask	0.0246	0.0424	0.0806	0.101	0.122	0.151

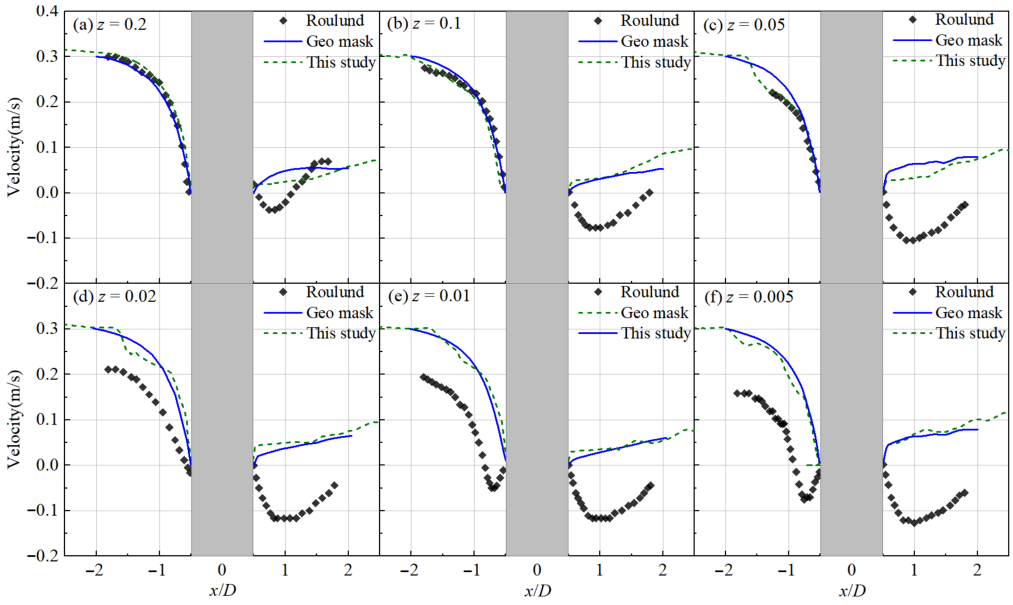


Figure 6. Validation of the structural drag method: comparison between numerical and experimental results.

To further assess the validity of the proposed approach within a numerical modelling framework, the simulated wake velocity distributions and their spatial evolution were compared with results obtained using a geometric masking (geo-mask) method, which was also implemented within the TELEMAC framework. A reasonable agreement between the numerical approaches indicates that, in large-scale hydrodynamic modelling, the structural drag source-term method can reasonably capture the main features of the wake structure and associated momentum dissipation. The MAE values range from 0.009 to 0.0166 m/s (Table 4), providing an objective measure of the consistency between the results of this study and the geo-mask data (numerical simulation result). It should be noted that the discrepancies observed in the downstream near-wake region and in the near-bed layer are not attributable to numerical instability or implementation errors. Instead, they arise from the parameterized nature of the structural drag source-term approach, which represents the monopile through an equivalent momentum source without explicitly resolving fine-scale processes such as flow separation, vortex shedding, and shear-layer development. Consequently, a close quantitative match with high-resolution CFD simulations or laboratory measurements in terms of near-field flow details is not expected. These discrepancies, therefore, reflect the inherent limitations of large-scale parameterized models when applied to strongly three-dimensional and boundary-layer-dominated flows. Accordingly, the drag-related parameters used in the structural drag source-term approach, including the drag coefficient and the kernel width, were selected based on the idealized monopile validation against laboratory measurements, to ensure that the overall momentum loss induced by the monopile is reasonably represented in an integrated sense rather than to match detailed local velocity profiles.

Table 4. Mean Absolute Error (MAE, unit: m/s) between the present drag source-term model and the geo-mask model.

Grid List	Z = 0.2	Z = 0.1	Z = 0.05	Z = 0.02	Z = 0.01	Z = 0.005
This study	0.0162	0.0166	0.0166	0.0122	0.009	0.0140

Overall, by preserving the monopile-induced momentum loss in an integrated sense, the proposed method provides a physically consistent representation of the hydrodynamic

response at its intended modelling scale. Although the local-scale validation is conducted using a single monopile configuration, it primarily serves to verify the physical consistency and numerical stability of the structural drag source-term formulation. At the array and regional scales, where the flow response is governed by the spatial superposition of identical source terms and large-scale momentum balance. The validated single-structure behavior provides a necessary physical basis for its extension to the wind farm array. At these larger spatial scales, where the hydrodynamic evolution is primarily governed by large-scale momentum balance and dissipation rather than instantaneous vortex dynamics, the structural drag source-term approach offers a theoretically coherent and computationally efficient modelling strategy. The extension from a single monopile to an array configuration is physically justified because the present model represents pure drag-induced momentum loss from individual monopiles, without involving any energy conversion process. The drag force acting on each monopile is governed by local flow conditions and remains fundamentally consistent, even in the presence of array-induced flow interactions. Consequently, the drag coefficient calibrated from the single monopile validation can be directly applied in the array-scale simulations. In this study, C_D is set to 0.3, which falls within the typical range reported for cylindrical monopiles under high Reynolds number flow conditions. This value accounts for the spatial spreading of the drag force through the kernel function, avoiding an overestimation of momentum loss that would occur if using the full-scale drag coefficient of an isolated monopile. It should be noted that the present approach is not intended to replace high-resolution CFD simulations for detailed near-field flow analysis, but rather to efficiently represent structural effects within large-scale hydrodynamic models.

Based on the above validation results, the structural drag source-term approach shows good applicability and physical consistency across scales. In the idealized monopile test, the simulated flow field agrees well with experimental measurements, confirming its reliability at the local scale. In the field validation, the model simulates tidal elevations and current variations with good accuracy, indicating good performance under complex boundary conditions and time-varying tidal forcing. Overall, the method exhibits consistent hydrodynamic behavior, supporting its application in the wind turbine monopile array simulations and regional-scale impact assessments.

4. Result and Discussion

To investigate the hydrodynamic impact of the array on the overall flow field, numerical simulations were conducted under representative tidal conditions. The diameter of the wind turbine monopile foundation was determined with reference to the engineering scale of typical large offshore wind turbines [32], and a representative value of 10 m was adopted. The simulation period extended from 8 August to 22 August 2024, covering a total of 15 days and spanning a complete neap-spring tidal cycle, thereby enabling the periodic variation in tidal current intensity across different tidal phases to be adequately captured. Additionally, the first three days of the simulation were considered a model spin-up period.

4.1. Overall Flow Response to the Wind Farm

This section describes the tidal elevation and current fields in the eastern coastal waters of the Shandong Peninsula based on simulations with the array deployed, providing an overall hydrodynamic context for the analysis of flow responses at different spatial scales. The array considered in this study consists of 80 monopiles arranged in a regular 8×10 layout at the engineering scale, and the present section focuses on the overall flow response of the array as a whole. The detailed geometric layout and numbering scheme are introduced in Section 4.2.1. The spring and neap tidal stages were classified according to

the astronomical tidal cycle (i.e., the lunar phase method). Representative instants were then selected near the peak current velocities during the flood and ebb phases.

4.1.1. General Characteristics of the Flow Field

Figure 7 presents the spatial distributions of tidal elevation and current velocity fields, with flow directions superimposed, at representative instants during spring and neap tides. Overall, the tidal current intensity during spring tides is significantly higher than that during neap tides. Specifically, as shown in Figure 7a,b, the spring flood and ebb stages are characterized by relatively strong currents, with instantaneous domain-averaged velocities of 0.478 m/s and 0.470 m/s, respectively. During neap tides (Figure 7c,d), the tidal current intensity is substantially reduced, with the instantaneous domain-averaged velocities decreasing to 0.308 m/s and 0.281 m/s, respectively. Similarly, tidal elevation shows a larger amplitude during spring tides than during neap tides, whereas its spatial distribution remains broadly similar across tidal stages. This indicates that tidal elevation primarily acts as a regional background water-level variation, without introducing pronounced spatial heterogeneity across the study area.

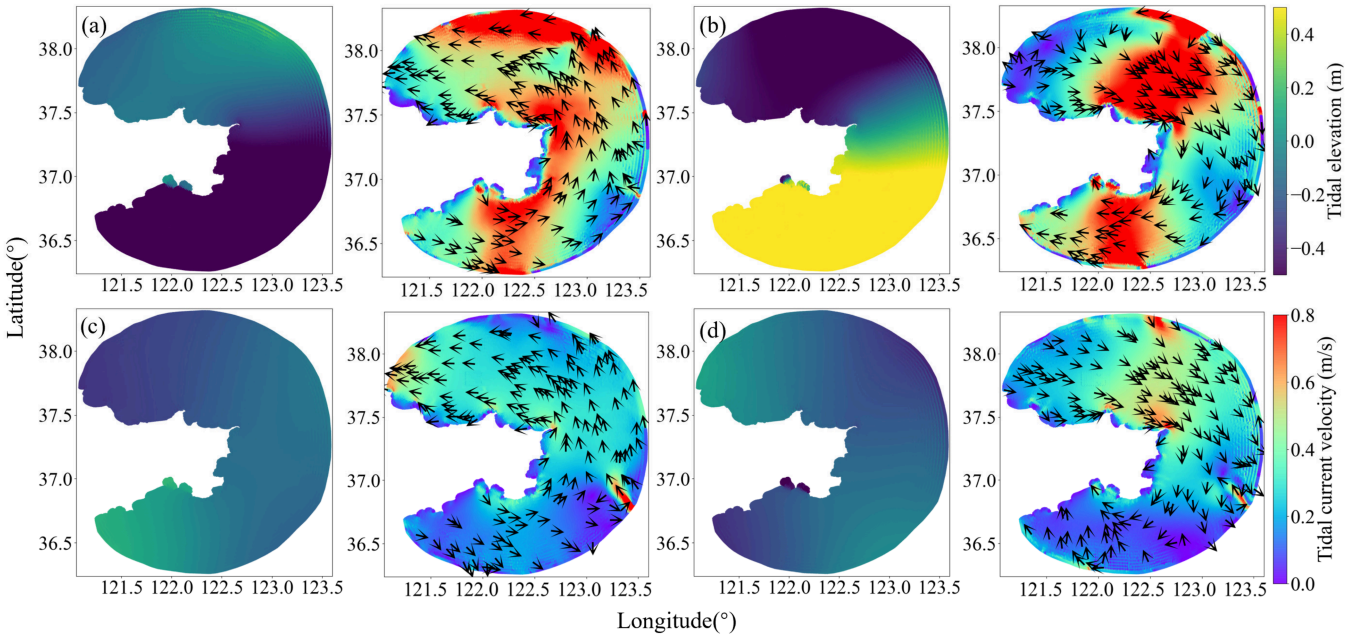


Figure 7. Spatial distributions of tidal elevation and tidal current velocity fields under different tidal conditions: (**a**) spring flood at 12:00 on 21 August 2024, (**b**) spring ebb at 19:00 on 21 August 2024, (**c**) neap flood at 04:00 on 14 August 2024, and (**d**) neap ebb at 11:00 on 14 August 2024.

4.1.2. Array-Scale Wake Structures

Figure 8 shows the tidal current velocity fields at both the array scale and representative monopile locations. At the array scale (Figure 8a), a clear spatial gradient of background tidal current velocity is observed, increasing gradually from the nearshore region toward offshore areas, with localized low-velocity wake regions forming downstream of individual monopiles along the dominant flow direction. The black square marks the representative area selected for detailed local inspection (zoomed in). Figure 8b–e presents the local velocity fields at a representative monopile location at characteristic instants selected near the peak current velocities during the spring flood, spring ebb, neap flood, and neap ebb stages, respectively. The results show that, at these representative near-peak instants, monopile wakes appear as coherent low-velocity regions extending downstream under different tidal stages.

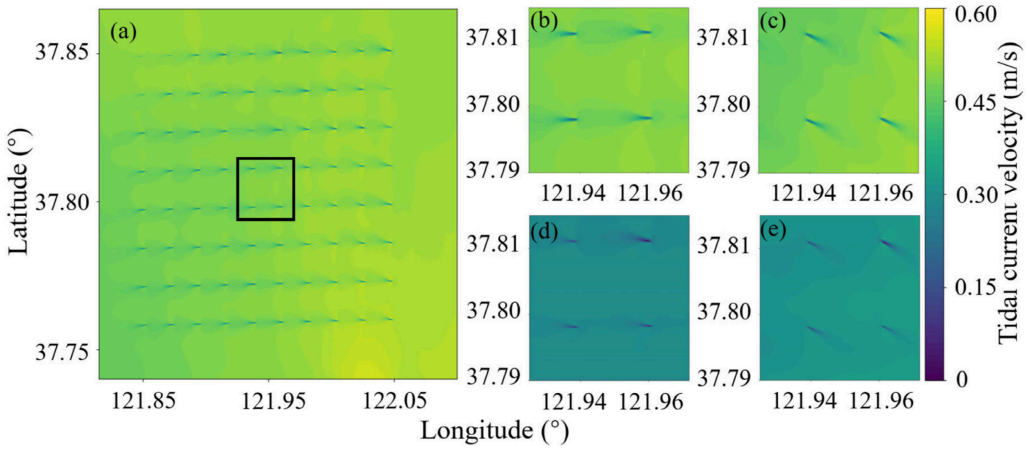


Figure 8. Array-scale tidal current velocity field and zoomed-in wake structures at representative monopile locations at characteristic instants near the peak current velocities: (**a**) array-scale velocity field including all 80 monopiles; (**b**) spring flood; (**c**) spring ebb; (**d**) neap flood; and (**e**) neap ebb.

During spring tides, although the absolute velocities within the wake regions remain relatively high, the velocity deficits relative to the incoming flow are more pronounced, making wake structures more clearly identifiable and spatially extensive. In contrast, under neap tide conditions, the weaker background currents result in reduced relative velocity deficits and weaker wake-induced disturbances, causing wake features to appear less distinct and more spatially confined. In addition, during flood and ebb phases, the downstream extension of the wake aligns with the dominant tidal flow direction. Overall, these observations indicate that the prominence of monopile wake structures is influenced not only by the absolute velocity levels within the wake regions, but also by the relative contrast with the background inflow.

4.1.3. Array-Induced Normalized Velocity Response

The array-scale wake structures discussed in Section 4.1.1 primarily illustrate the spatial patterns of tidal current velocity under different tidal conditions, but do not provide a direct quantitative measure of the magnitude of array-induced flow modification relative to the free-field condition. To facilitate a consistent and quantitative comparison among different tidal regimes, a normalized velocity metric is introduced. This metric is defined as the relative deviation of the flow velocity under array conditions from the corresponding free-field velocity and is expressed in percentage form. Positive and negative values indicate relative velocity enhancement and reduction, respectively. This formulation provides a unified, normalized measure of array-induced flow modulation. The normalized velocity change is defined as follows:

$$\Delta U_{norm}(\%) = \frac{U_{array} - U_{free}}{U_{free}} \times 100\% \tag{13}$$

where U_{array} and U_{free} denote the flow velocity under wind turbine monopile array and free-field conditions at the same spatial location, respectively. In this study, the velocity magnitude used in the calculation is time-averaged over the spring tide period and the neap tide period, respectively.

As shown in Figure 9, both spring and neap tidal conditions exhibit clear and consistent response of the flow field to the presence of the array. Specifically, under both tidal regimes, the normalized velocity change reaches comparable percentage levels, with localized extrema of approximately −10% occurring in the wake regions downstream of individual monopiles. Despite the similarity in extreme values, the normalized velocity response

under both spring and neap tide conditions remains primarily concentrated in the near-wake regions downstream of individual monopiles. The quantitative results corroborate the qualitative observations presented in Section 4.1.1, indicating that the two tidal regimes differ primarily in the wake contrast with respect to the background flow rather than in their spatial extent.

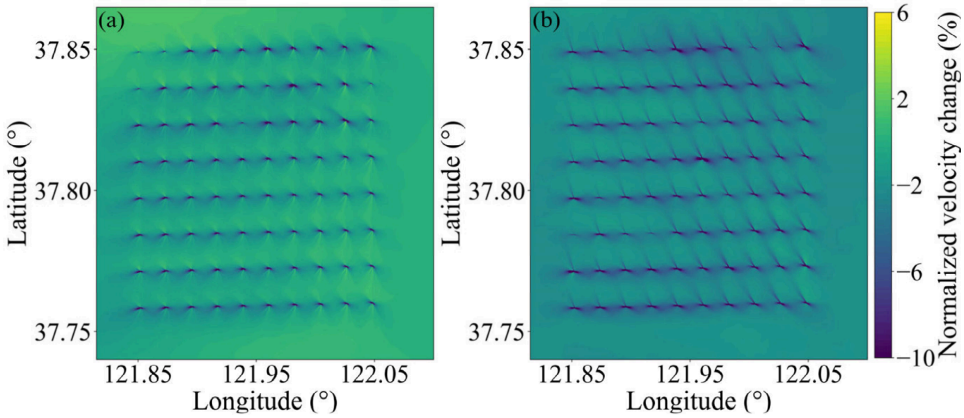


Figure 9. Array-induced normalized velocity change under (**a**) spring and (**b**) neap tidal conditions.

In general, positive changes on the order of 0% to +3% are widely distributed within the inter-row and peripheral areas of the array under spring tide conditions, resulting in a heterogeneous spatial pattern of coexisting positive and negative responses. Under neap tide conditions, the normalized velocity change within the array domain exhibits a more uniform and unidirectional pattern, with large portions of the array area being continuously dominated by negative changes, typically ranging from −3% to −8%. In contrast, regions exhibiting positive changes are significantly reduced in both spatial extent and frequency. Overall, spring and neap tides differ not in the peak normalized velocity change, but in the spatial organization and coherence of the response, as well as the relative dominance of positive and negative changes within the array domain.

4.2. Array-Induced Velocity Response Characteristics

The deployment of wind farm arrays not only alters local flow velocity but also induces velocity responses with distinct spatial structures and temporal evolution. As the array-induced velocity variations are influenced by downstream distance, array geometry, and background tidal conditions, a single spatial scale or physical quantity is insufficient to characterize the response. Therefore, a systematic analysis from both spatial and temporal perspectives is conducted to elucidate the spatial distribution, along-stream evolution, and temporal response of the array-induced velocity field.

4.2.1. Layout of the Wind Farm Array

The geometric layout of the array, together with the numbering scheme and sampling definitions, is illustrated in Figure 10. The left and right sides correspond to fixed geographical directions in the map view and represent purely geometrical positions in the layout, rather than being defined with respect to the dominant flow or downstream direction. This array consists of 8 transverse rows and 10 columns, and the rows are labeled from Line A to Line H from top to bottom. Monopiles are numbered starting from the upper-right corner of the array in the map view as monopile No. 1 and continue sequentially along the column direction.

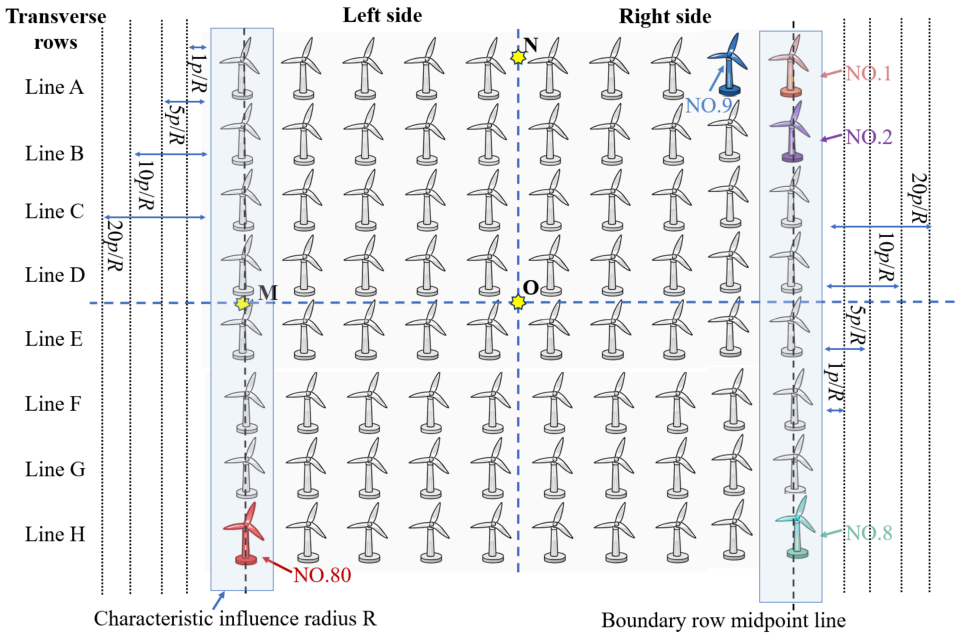


Figure 10. Schematic of the wind farm array layout and definition of sampling locations.

The longitudinal midpoint line of the outermost monopile column is taken as a reference baseline. The sampling distance R_{kernel} is defined as the lateral distance from the reference baseline to a given sampling location. It represents the characteristic spatial scale of the kernel function used to distribute the drag force induced by individual structures into the surrounding flow field. This parameter controls the lateral extent over which the structural resistance is applied, thereby ensuring a continuous representation of the array-induced drag effect. In the present study, R_{kernel} is set to 10 m, corresponding to the characteristic diameter of the monopile (e.g., 15 MW, D = 10 m) [33]. This choice ensures that the spatial extent of the distributed drag force remains physically consistent with the structural scale, thereby localizing the momentum loss around each monopile. For brevity, R is used to denote R_{kernel} in the following contents. The downstream distance p is measured from the same baseline along the dominant flow direction.

The dimensionless distance p/R is then used to describe the relative spatial positions of different downstream sampling locations, with p/R = 1, 5, 10, and 20 corresponding to near-field to far-field regions, respectively. These distances approximately represent the near-wake region ($p/R \approx 1$), transition zone to the far-wake ($p/R \approx 5$), the far-wake recovery region ($p/R \approx 10$) and the far field region ($p/R \approx 20$). This selection ensures that the full spatial evolution of the flow disturbance induced by the array is captured. Moreover, the chosen range is broadly in line with wake recovery behavior reported in studies of flow past bluff bodies and offshore wind turbine arrays [34–37]. It should be noted that under realistic tidal conditions, the flow direction reverses between the flood and ebb phases. Consequently, the upstream and downstream directions are not fixed in space, and a given geometrical side of the array may correspond to an upstream position during one phase and a downstream position during another. Accordingly, both geometrical sides of the array are considered to ensure a comprehensive characterization of the array-induced velocity response under reversing tidal flows. Point O denotes the geometric center of the array, while points M and N are located at representative positions along the outermost monopile on either side of the array. These points are selected as characteristic sampling locations for subsequent velocity time-series analysis.

4.2.2. Spatial Distribution of Array-Induced Velocity Response

Figures 11 and 12 illustrate the variations in time-averaged velocity magnitude along the array transverse rows (Lines A–H) at different downstream distances (p/R = 1, 5, 10, and 20) under spring and neap tidal conditions, respectively. For a given downstream distance, the velocity variation patterns along the array rows on the left and right sides of the array are generally similar along lines A–H, indicating a similar overall trend in the array-induced response. At the row-wise local scale, pronounced velocity attenuation is observed at the rows corresponding to monopile locations. As the incoming flow passes through a monopile row, the velocity decreases rapidly due to wake effects, while smoother and gradually recovering velocity profiles are observed in the inter-row regions. Quantitatively, under spring tide conditions, the velocity deficit (defined relative to the no-turbine case at the same location) at p/R = 1, 5, 10, and 20 on the left side is 37.9%, 17.2%, 10.3%, and 6.9%, respectively; on the right side, the deficits are 22.2%, 11.1%, 5.5%, and 1.4%, respectively. Under neap tide conditions, the corresponding deficits on the left side are 25%, 15.6%, 9.4%, and 3.1%, and on the right side are 22.2%, 8.3%, 4.4%, and 1.1%. This behavior reflects momentum dissipation by the monopiles and the subsequent velocity recovery driven by turbulent mixing and lateral transport. Therefore, the spatial structure of the velocity modulation is primarily governed by the overall array configuration rather than by lateral asymmetry in the flow field.

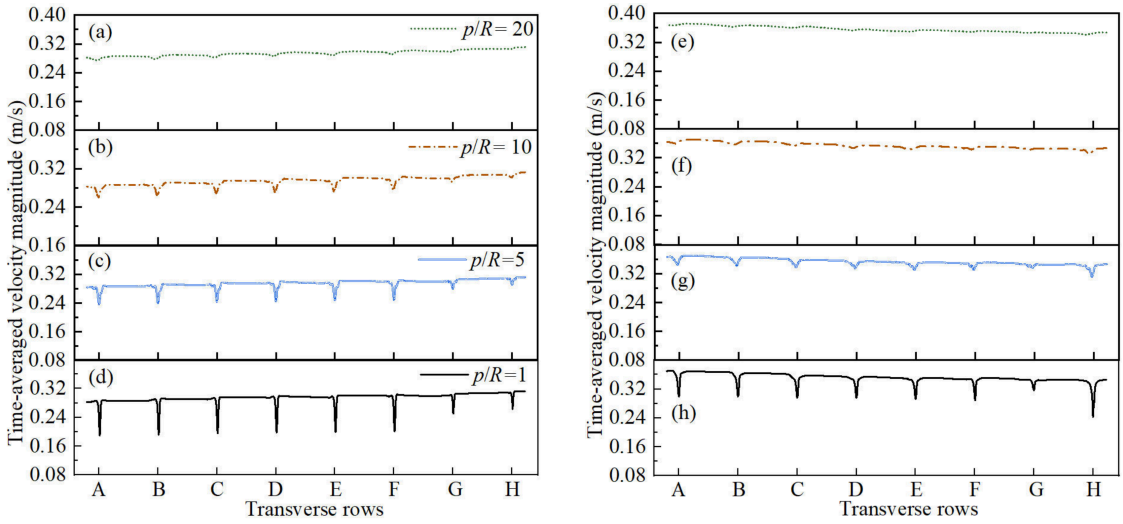


Figure 11. Spatial characteristics of array-induced velocity modulation behind monopile foundations under spring tidal conditions (**a**–**d**) left side, p/R = 1, 5, 10, 20; (**e**–**h**) right side, p/R = 1, 5, 10, 20.

A comparison between spring and neap tidal conditions indicates that, although the overall velocity patterns remain similar, spring tide exhibits larger modulation amplitude. For example, at the inter-row region at p/R = 1, the velocity is 0.28 m/s under spring tide versus 0.16 m/s under neap tide, a 75% increase. This suggests that tidal intensity primarily affects the strength of the array-induced modulation, without altering its fundamental spatial structure. To quantify downstream recovery, the recovery length scale defined as the distance where the velocity deficit falls below 10%. This threshold is adopted as a practical criterion to enable consistent comparison of recovery distances under different tidal conditions. Using the linear interpolation method, the recovery distances under spring tide are $p/R \approx 11$ and $p/R \approx 6$ on the left and right side, respectively. While under neap tide conditions it reduces to about $p/R \approx 9.5$ (left) and $p/R \approx 4.5$ (right). These results indicate a faster recovery of velocity on the right side of the array and under weaker tidal forcing. The shorter recovery length under neap tide conditions is primarily attributed to

the smaller initial velocity deficit associated with weaker tidal forcing, which allows the velocity deficit to fall below the threshold over a reduced downstream distance.

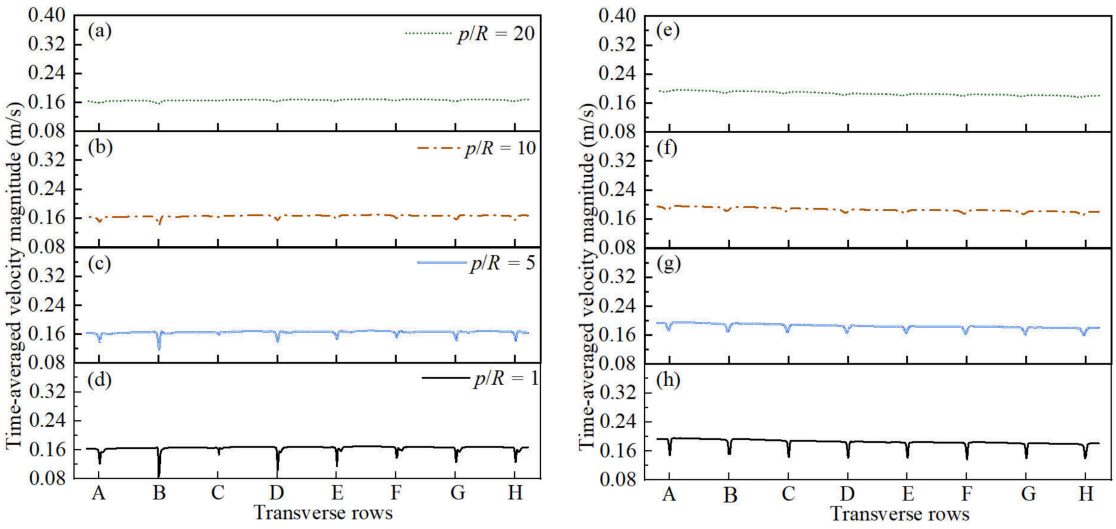


Figure 12. Spatial characteristics of array-induced velocity modulation behind monopile foundations under neap tidal conditions (**a**–**d**) left side, p/R = 1, 5, 10, 20; (**e**–**h**) right side, p/R = 1, 5, 10, 20.

4.2.3. Spatial Decay and Recovery of Velocity Deviation

As Figure 13 shows, from the perspective of downstream evolution, pronounced periodic fluctuations in velocity are observed in the near-field region (p/R = 1) along the transverse direction, with distinct velocity deficits about the troughs occurring at locations corresponding to the monopiles. The array-induced velocity deviations exhibit clear negative peaks with magnitudes on the order of 10^{-2} m/s. This denotes that the local flow field is primarily influenced by the direct effect of wakes generated by individual monopile rows. As the downstream distance increases to p/R = 5 and 10, the amplitude of velocity modulation gradually decreases, and the overall distribution becomes smoother, with reduced transverse gradients and weakened periodic fluctuations. Meanwhile, the recovery process exhibits spatial non-uniformity, with faster velocity recovery occurring in the inter-row regions compared with the monopile-row locations, indicating a progressive weakening of wake effects during downstream propagation. When the downstream distance further increases to p/R = 20, the velocity variations along the transverse direction are substantially reduced. The residual velocity deviation is confined to a very small range within $\pm$ 0.005 m/s. This indicates that the influence of the array on the velocity structure is significantly weakened at this downstream distance. However, weak periodic features associated with the array geometry can still be identified, suggesting that residual array wakes retain spatial organization in the mid- and far-field.

The time-averaged results show that the velocity deviation distributions on the left and right sides of the array remain consistent at all downstream distances. This symmetry reflects that, under tidal current forcing, instantaneous upstream-downstream asymmetries induced by the array are effectively mitigated through flow reversal, resulting in an overall symmetric spatial pattern of velocity modulation. Nevertheless, small local differences between the two sides can still be observed. These residual asymmetries are likely attributable to inherent differences between flood and ebb tidal conditions, including variations in peak velocity, duration, and acceleration characteristics, as well as background flow non-uniformity. Such differences remain minor compared with the dominant symmetric response induced by flow reversal.

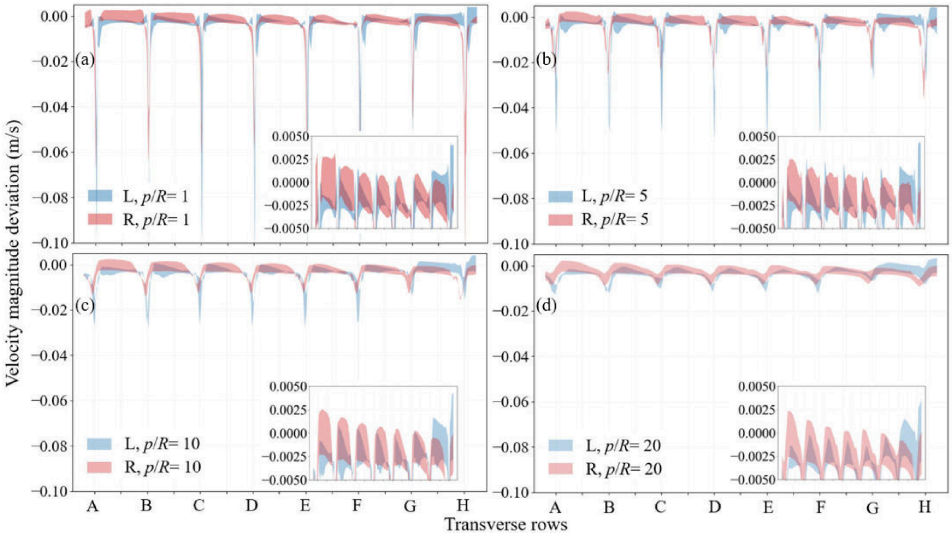


Figure 13. Spatial decay and recovery of array-induced velocity magnitude deviation along the array rows at different downstream distances (**a**) p/R = 1; (**b**) p/R = 5; (**c**) p/R = 10; (**d**) p/R = 20.

4.2.4. Temporal Response of Velocity at Representative Locations

To further examine the temporal characteristics of the array-induced velocity response, velocity time series at several representative locations are analyzed. These locations correspond to the representative points previously defined in Figure 10, namely the array center (O) and two characteristic positions (M and N) along the boundary monopile columns.

The velocity time series at the representative locations exhibit consistent tidal periodicity and aligned phases across multiple consecutive tidal cycles (Figure 14), indicating that the deployment of the array does not alter the fundamental temporal structure of the tidal flow. Instead, the array influence is expressed as a stable modulation of velocity amplitude, representing a persistent background effect rather than a transient response. Although spring tides are associated with higher velocity levels and stronger modulation amplitudes than neap tides, the relative temporal behavior among the representative locations remains consistent. From a single-point time-series perspective, the array-induced modulation therefore appears more pronounced during spring tides, whereas under neap tidal conditions, it is smoother and partially masked by the weaker background flow.

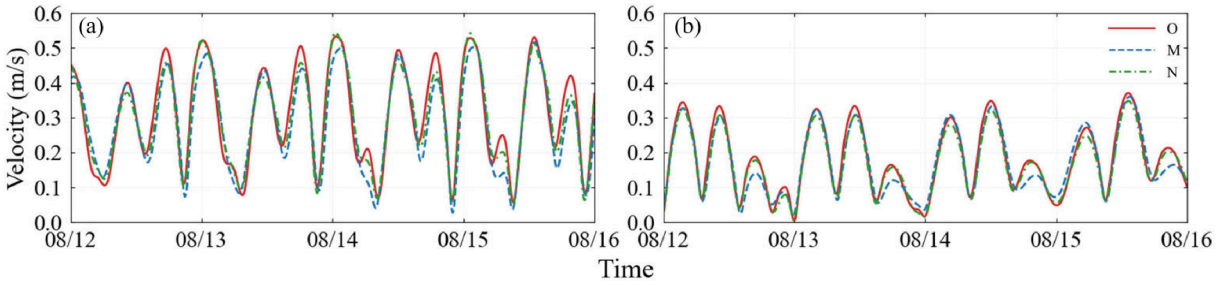


Figure 14. Spatial decay and recovery of array-induced velocity magnitude deviation along the array rows at different downstream distances (**a**) spring tidal conditions; (**b**) neap tidal conditions.

Although some differences in velocity magnitude can be observed among the representative locations, the overall temporal variations exhibit similar tidal oscillations with aligned trends. However, the magnitude differences remain minor, as the selected locations are not situated within the immediate near-wake cores of individual monopiles. Moreover, under tidal current forcing, periodic flow reversal further smooths local asymmetries over time, reducing the apparent strength of array-induced effects in single-point velocity time

series. As a result, the temporal response at individual locations reflects a comparatively weak but consistently present modulation induced by the array.

4.3. Array-Induced Modulation of Flow Kinetic Energy

Although the velocity-based analyses presented above provide detailed insights into the local and array-scale flow responses, velocity by itself cannot fully represent the integrated energetic impact of the array on the flow system. Therefore, a system-scale perspective based on spatially averaged flow kinetic energy is adopted to quantify the integrated impact of the array, with particular emphasis on its radial variation from the array center. At this scale, the array primarily influences the flow through cumulative momentum dissipation associated with foundation-induced drag and wake effects. Consequently, monopile foundations act as distributed drag source that redistribute and dissipate flow kinetic energy. Here, kinetic energy density is employed as a diagnostic measure rather than a representation of energy extraction.

4.3.1. Spatial Distribution of Kinetic Energy Density

The flow kinetic energy density is calculated based on the time-averaged value over the selected period. It is defined as

$$KE = \frac{1}{2}\rho_{water}\overline{\overline{u}^2 + \overline{v}^2} \tag{14}$$

where $\overline{u}$ and $\overline{v}$ denote the depth-averaged horizontal velocity components, the overbar indicates time averaging.

To quantitatively characterize the overall energy state of the array region, two metrics are considered. The area-averaged kinetic energy density and total kinetic energy of the array region, both derived from the time-averaged kinetic energy density field. The former represents the mean kinetic energy density within the array coverage, while the latter quantifies the total kinetic energy obtained by spatial integration over the same region. Their expressions are given as follows:

$$\overline{KE_{array}} = \frac{1}{A_{array}}\int_{A_{array}} KE dA \tag{15}$$

$$KE^{tot}_{array} = \int_{A_{array}} KE dA \tag{16}$$

where KE denotes the time-averaged kinetic energy density, A_{array} represents the horizontal area covered by the array, and the integration is performed over the array region in the horizontal plane.

Based on the definitions given above, the area-averaged and the total kinetic energy of the array region are quantified for spring and neap tidal conditions. As Figure 15 shows, in tidal spring conditions, the time-averaged kinetic energy density within the array-covered region is approximately 141.057 J/m^3, and the corresponding area-integrated kinetic energy is about 4.48×10^{12} J/m, indicating that both the overall energy level and the energy scale within the array region remain relatively high. In contrast, under neap tide conditions, the mean kinetic energy density within the array-covered region decreases to approximately 27.396 J/m^3, with a corresponding area-integrated kinetic energy of about 8.71×10^{11} J/m, suggesting a pronounced reduction in both the energy level and the energy scale within the array region under neap tidal conditions compared with spring tides.

From a spatial distribution perspective, despite the pronounced differences in absolute kinetic energy density levels between spring and neap tide conditions, the array-induced patterns of kinetic energy density remain structurally consistent. Low-energy regions

are predominantly associated with the monopile locations and their surrounding wake areas, exhibiting a clear spatial organization aligned with the monopile layout and forming localized deficits with elongated wake-like features along the dominant flow direction. Because the absolute magnitude of kinetic energy density varies considerably between tidal conditions, different color scales are used to highlight the internal spatial distribution in each case, and these scales are not intended for direct comparison of absolute values.

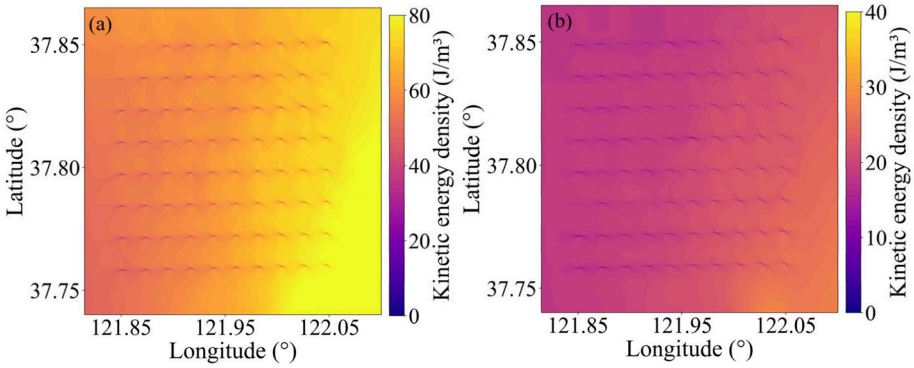


Figure 15. Array-induced modulation of kinetic energy density under (**a**) spring and (**b**) neap tidal conditions.

4.3.2. Radial Extent of Array Effects

To quantitatively characterize the influence of the array on flow kinetic energy, a radial analysis framework centered on the array centroid is established in the horizontal plane, based on which a characteristic array scale is introduced.

As shown in Figure 16, the array characteristic radius R_{array} is defined as half of the diagonal length of the geometric envelope enclosing all monopiles in the array. The selected bin width represents a reasonable balance between spatial resolution and statistical robustness, enabling the capture of local flow features while maintaining sufficient samples within each annular bin. Specifically, half of the inter-turbine spacing is adopted to ensure that the annular averaging scale remains smaller than the turbine spacing, thereby resolving the gradual radial variation of array-induced effects without excessive spatial smoothing. Based on this characteristic scale, a core region is defined within the array to represent a representative source region of momentum dissipation. This core region is located inside the geometric boundary of the array and is selected to characterize the superposition effects of multiple monopile foundations. By focusing on the interior of the array, where edge-related bypass flow and ambient-fluid compensation are minimized, allowing for a more representative and approximately additive assessment of array-induced momentum dissipation. Accordingly, a radial extent of 0.3 R_{array} is adopted to define the core area.

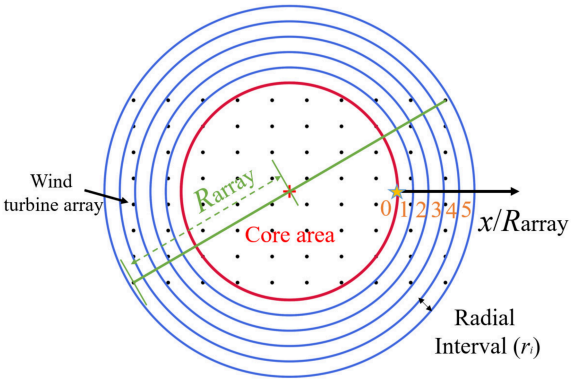


Figure 16. Schematic of the array-centered radial analysis and definition of the core region.

As illustrated in Figure 16, a series of concentric annular bins centered on the array centroid is constructed in the horizontal plane to evaluate array-induced effects as a function of radial distance statistically. This annular averaging framework enables a direction-independent quantification of the spatial modulation imposed by the array as an integrated structure, without introducing assumptions regarding a preferred flow direction. It is therefore particularly suitable for tidal environments with temporally varying flow directions. However, it should be noted that tidal currents exhibit pronounced directional characteristics associated with alternating flood and ebb phases, and wake structures may differ under different flow directions. In this context, the radial averaging method should be interpreted as a statistical spatial averaging approach rather than a representation of directional flow variations. Although this method inevitably weakens directional wake features, it remains effective for characterizing array-scale averaged effects. Accordingly, within each annular bin, the array-induced energetic response is quantified using the radially averaged relative kinetic energy variation, defined as Equation (17):

$$\left\langle \overline{KE} \right\rangle^{(c)}(r_i) = \frac{1}{A_{r_i}} \int_{A_{r_i}} \overline{KE}^{(c)}(x,y)dA \tag{17}$$

where A_{ri} denotes the area of the annular region corresponding to the i-th radial interval centered at r_i, c denotes the test condition, corresponding to the array and free-field cases.

In this study, the radial interval is set to 850 m based on the characteristic spacing between adjacent monopiles in the array, with the typical transverse inter-monopile distance being approximately 1700 m. It should be noted that the selected annular-bin width is introduced solely for statistical analysis and does not represent a physical decay length of the array-induced effects.

Based on radially averaged kinetic energy defined (Equation (17)), the relative change in kinetic energy density with respect to the free-field condition, ΔKE, is defined in Equation (18). This metric is employed to quantify the relative energetic modulation imposed by the array on the flow system.

$$\Delta KE = \frac{\left\langle \overline{KE} \right\rangle^{(array)}(r_i) - \left\langle \overline{KE} \right\rangle^{(free)}(r_i)}{\left\langle \overline{KE} \right\rangle^{(free)}(r_i)} \tag{18}$$

where $\overline{KE}^{(array)}$ and $\overline{KE}^{(free)}$ corresponds to the array and free-field cases, respectively.

Figure 17 presents the variation of ΔKE as a function of the normalized radial distance from the array center, x/R_{array}. ΔKE increases with radial distance and reaches a maximum at approximately $x/R_{array} \approx 2.2$ during spring tides and ≈2.7 during neap tides. This behavior suggests that the relative reduction in flow kinetic energy induced by the array is not confined to the source region associated with array-induced momentum dissipation, but progressively manifests during the radial expansion of array-induced disturbances. This radial range reflects the location where array-induced disturbances accumulate during radial expansion, resulting in the maximum deviation from the free-field condition. With further increases in radial distance, ΔKE exhibits an overall decreasing trend. This indicates that the relative energy perturbations induced by the array are progressively compensated through lateral momentum exchange and wake diffusion, and that the flow field gradually recovers toward the free-field state. It should be noted that the radial location of the maximum ΔKE does not necessarily coincide with the core region, as the core region is defined for statistical representativeness rather than to fully capture all monopile-induced momentum dispersion. This definition avoids the influence of bypass and compensating flows near the array boundary, enabling a clearer assessment of the array-scale energetic modulation.

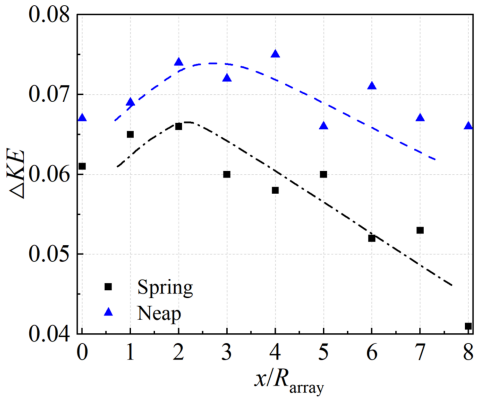


Figure 17. Radial variation of the relative kinetic energy change (ΔKE) induced by the monopile array under spring and neap tidal conditions.

A comparison between different tidal conditions shows that the radial variation of ΔKE exhibits a generally consistent pattern, while differences arise in the decay rate and the spatial extent of the array influence. Under spring-tide conditions, ΔKE decreases more rapidly with radial distance following its peak, even after normalization by the free-field kinetic energy. This behavior is consistent with a more efficient attenuation of array-induced disturbances under stronger background flows, where advection and lateral momentum redistribution by the ambient flow are more pronounced. In contrast, under neap-tide conditions, the peak value of ΔKE is relatively higher and remains significant over a larger radial range, suggesting that the relative modulation imposed by the array on the flow system is more pronounced under weaker flow conditions, leading to an expanded spatial influence.

5. Conclusions

This study investigates the array-scale hydrodynamic impacts of a dense offshore wind farm array on tidal flow and energy redistribution using an established drag-based source-term formulation implemented through a dedicated module within the TELEMAC-3D framework. The background hydrodynamics are validated against measured tidal elevation and current velocity data from field stations, demonstrating the model's capability to simulate realistic tidal flow conditions. The structural drag source-term formulation is further evaluated through comparison with published numerical and experimental results for a monopile, demonstrating that the approach can capture physically consistent flow features. By constructing a representative large-scale monopile array in a tidal channel, the flow structure, velocity response, and kinetic energy modulation induced by the array were systematically analyzed under spring-neap tidal conditions. The main conclusions are summarized as follows:

(1) The implemented drag-based source-term formulation represents the hydrodynamic effects of offshore wind farm arrays within a regional-scale modeling framework under realistic tidal conditions. By parameterizing monopile-induced drag, the method captures the integrated hydrodynamic response at the regional scale, enabling simulations of dense monopile arrays.

(2) At the array scale, the monopile array induces a relatively moderate modulation of the large-scale tidal flow, while its influence remains spatially extensive. Array-induced velocity and energy perturbations are primarily concentrated in the vicinity of the array but extend to distances of approximately $p/R \approx 20$, beyond which the flow gradually recovers toward free-field conditions.

(3) The deployment of the monopile array does not alter the fundamental temporal structure of the tidal flow, which remains characterized by consistent periodicity and phase alignment. Instead, the array influence is manifested primarily as a modulation of velocity amplitude, the magnitude of which varies with tidal intensity. This modulation is more pronounced during spring tides and comparatively weaker during neap tides, with localized relative velocity variations on the order of 10% occurring under spring tidal conditions. Despite these differences in magnitude, the overall temporal behavior and spatial structure of the array-scale response remain largely similar across representative locations.

(4) The presence of the monopile array induces a systematic redistribution of flow kinetic energy, characterized by a reduction within the array region and a gradual recovery toward free-field conditions with increasing radial distance. This pattern reflects the spatial reorganization of kinetic energy under array-scale drag forcing.

Overall, the present approach can efficiently simulate the array-scale hydrodynamic and capture the energetic responses of offshore wind farms under tidal flow conditions. However, validation at the array scale remains limited and requires further investigation. In addition, it should be noted that, in this study, monopiles are represented through an equivalent structural drag formulation with simplified and spatially uniform parameterization, and additional effects associated with rotor-induced flow and energy extraction are not considered. Furthermore, the present study focuses on tidal-current-driven hydrodynamics and does not account for wave–current interactions or sediment transport processes. Incorporating these aspects in future studies would further broaden the applicability of the present approach.

Author Contributions: F.W.: Data Curation, Formal Analysis, Funding Acquisition, Investigation, Methodology, Visualization, Writing—Original Draft. D.L.: Formal Analysis, Validation, Resources, Supervision, Writing—Review and Editing. J.Z.: Conceptualization, Funding Acquisition, Resources, Supervision, Writing—Review and Editing. Y.G.: Conceptualization, Supervision, Validation, Writing—Review and Editing. H.C.: Review and editing, Software, Investigation, Formal analysis. All authors have read and agreed to the published version of the manuscript.

Funding: This research was funded by the Science and Technology Project of China Huaneng Group (HNKJ23-H18) and the Fundamental Research Funds for the Central Universities (No B240205039).

Data Availability Statement: Data are contained within the article. For further inquiries, please contact Fangyu Wang (fywang@hhu.edu.cn).

Conflicts of Interest: The authors declare that they have no known competing financial interests or personal relationships that could have appeared to influence the work reported in this paper.

Abbreviations

Symbol	Meaning
A-H	Array transverse rows
A_{fi}	Amplitude of variable f in the i-th harmonic component
A_{kern}	the support domain of the truncated Gaussian kernel
A_{ri}	Area of the i-th annular bin
A_{ref}	Reference area
C_D	Structural drag coefficient
D_{pile}	Pile diameter
d_{50}	Median sediment grain size
*E*1, *E*2, *E*3, *E*4, *E*5	Tidal elevation observation station
F_D	Structural drag force
F_x	Source terms of the fluid in the x direction

F_y	Source terms of the fluid in the y direction
F_z	Source terms of the fluid in the z direction
f	Water depth or one component of the horizontal velocity
$f_i(t)$	Nodal factor for the lunar modulation of tidal effects
$g_i(t)$	Nodal factor for the lunar modulation of tidal effects
i	Index of the tidal constituent
KE	Kinetic energy density
$\overline{KE_{array}}$	Area-averaged kinetic energy density
KE_{array}^{tot}	Total kinetic energy of the array region
$\langle \overline{KE} \rangle^{(c)}$	Radially averaged relative kinetic energy density
$\langle \overline{KE} \rangle^{(array)}$	Array cases kinetic energy density
$\langle \overline{KE} \rangle^{(free)}$	Free-field kinetic energy density
k_s	Nikuradse roughness height
M, N	Characteristic locations along the boundary monopile columns
O	Geometric center of the array
P_{pre}	Total pressure
P_{atm}	Atmospheric pressure
P_d	Hydrostatic pressure
p	Lateral distance from this baseline to a given sampling location
R_{kernel}	Spatial decay range of the drag field
R	Shorthand notation for R_{kernel}
R_{array}	Array characteristic radius
r	Horizontal distances from the pile center
r_i	Radial Interval
$S_{x,y}$	Horizontal component of the structural drag source term
T_i	Period of harmonic components
t	Time
U_0	Constant inflow velocity of the experimental setting
ΔU_{norm}	Normalized velocity change
U_{array}	Flow velocity under the wind turbine monopile array condition
U_{free}	Flow velocity under free-field condition
U_{in}	Local inflow velocity
$\mid U_{\mathrm{in}} \mid$	Magnitude of the local flow velocity vector U_{in}
U	Velocity components in the x direction
$\overline{u}$, $\overline{v}$	Depth-average velocity
V	Velocity components in the y direction
$V1$, $V2$, $V3$, $V4$, $V5$	Tidal velocity observation station
V_{ol}	Control volume over the integrated kernel function
V_d	Drag distribution volume
W	Velocity components in the z direction
$W(r)$	Kernel function
x	Horizontal direction
y	Horizontal direction
z	Vertical direction
z_{s}	Free surface elevation
β_{fi}	Phase of the variable f for the i-th constituent
${B^0}_i$	Initial phase
ρ_{water}	Water density
v	Kinematic viscosity
$\Delta(\cdot)$	Laplacian operator
σ	Sigma

References

1. IEA (International Energy Agency). *Offshore Wind Outlook 2024*; OECD/IEA: Paris, France, 2024. Available online: https://www.iea.org/reports/offshore-wind-outlook-2024 (accessed on 10 February 2026).
2. Cazenave, P.W.; Torres, R.; Allen, J.I. Unstructured grid modelling of offshore wind farm impacts in the Celtic Sea. *Prog. Oceanogr.* **2016**, *145*, 25–41. [CrossRef]
3. Carpenter, J.R.; Merckelbach, L.; Callies, U.; Clark, S.; Gaslikova, L.; Baschek, B. Potential Impacts of Offshore Wind Farms on North Sea Stratification. *PLoS ONE* **2016**, *11*, e0160830. [CrossRef]
4. Pacheco, A.; Ferreira, Ó. Hydrodynamic changes imposed by tidal energy converters on extracting energy on a real case scenario. *Appl. Energy* **2016**, *180*, 369–385. [CrossRef]
5. Sumer, B.M.; Fredsøe, J. The mechanics of scour in the marine environment. In *Advanced Series on Ocean Engineering*; World Scientific: Singapore, 2002; Volume 17.
6. Roulund, A.; Sumer, B.M.; Fredsøe, J.; Michelsen, J. Numerical and experimental investigation of flow and scour around a circular pile. *J. Fluid Mech.* **2005**, *534*, 351–401. [CrossRef]
7. Dixen, M.; Sumer, B.M.; Fredsøe, J. Numerical and experimental investigation of flow and scour around a half-buried sphere. *Coast. Eng.* **2013**, *73*, 84–105. [CrossRef]
8. Myers, L.E.; Bahaj, A.S. Experimental analysis of the flow field around horizontal-axis tidal turbines by use of scale mesh disk rotor simulators. *Ocean. Eng.* **2010**, *37*, 218–227. [CrossRef]
9. Yang, Z.; Wang, T.; Copping, A. Modeling tidal stream energy extraction and its effects on transport processes using a three-dimensional coastal ocean model. *Renew. Energy* **2014**, *68*, 373–385.
10. Neill, S.P.; Litt, E.J.; Couch, S.J.; Davies, A.G. The impact of tidal stream turbines on large-scale sediment dynamics. *Renew. Energy* **2009**, *34*, 2803–2812. [CrossRef]
11. Nishino, T.; Willden, R.H.J. The efficiency of an array of tidal turbines partially blocking a wide channel. *J. Fluid Mech.* **2012**, *708*, 596–606. [CrossRef]
12. Chen, L.; Zang, J.; Hillis, A.J.; Morgan, G.C.J.; Plummer, A.R. Numerical investigation of wave-structure interaction using OpenFOAM. *Ocean. Eng.* **2014**, *88*, 91–109. [CrossRef]
13. Nuernberg, M.; Tao, L. Experimental study of wake characteristics in tidal turbine arrays. *Renew. Energy* **2018**, *127*, 168–181. [CrossRef]
14. Strickland, J.; Stevens, R.J.A.M. Effect of thrust coefficient on the flow blockage effects in closely-spaced spanwise-infinite turbine arrays. *J. Phys. Conf. Ser.* **2020**, *1618*, 062069. [CrossRef]
15. Garrett, C.; Cummins, P. The efficiency of a turbine in a tidal channel. *J. Fluid Mech.* **2007**, *588*, 243–251. [CrossRef]
16. Vennell, R. Tuning tidal turbines in-concert to maximise farm efficiency. *J. Fluid Mech.* **2011**, *671*, 587–604. [CrossRef]
17. Vennell, R. The energetics of large tidal turbine arrays. *Renew. Energy* **2012**, *48*, 210–219. [CrossRef]
18. Funke, S.W.; Farrell, P.E.; Piggott, M.D. Tidal turbine array optimisation using the adjoint approach. *Renew. Energy* **2014**, *63*, 658–673. [CrossRef]
19. Coles, D.S.; Blunden, L.S.; Bahaj, A.S. Experimental validation of the distributed drag method for simulating large marine current turbine arrays using porous fences. *Int. J. Mar. Energy* **2016**, *16*, 298–316. [CrossRef]
20. Kramer, S.C.; Piggott, M.D. A correction to the enhanced bottom drag parameterisation of tidal turbines. *Renew. Energy* **2016**, *92*, 385–396. [CrossRef]
21. Rivier, A.; Bennis, A.-C.; Guillou, N.; Pinon, G.; Magar, V. Parameterization of wind turbine impacts on hydrodynamics and sediment transport. *Ocean. Dyn.* **2016**, *66*, 1285–1299. [CrossRef]
22. Stansby, P.; Ouro, P. Modelling marine turbine arrays in tidal flows. *J. Hydraul. Res.* **2022**, *60*, S1–S19. [CrossRef]
23. Zengler, C.P.; Troldborg, N.; Gaunaa, M. Modeling the influence of streamwise flow field acceleration on the aerodynamic performance of an actuator disk. *Wind. Energy Sci.* **2025**, *10*, 1485–1497. [CrossRef]
24. Hervouet, J.M.; Ata, R. *TELEMAC-3D Open-Source Software: User Manual*; EDF R&D: Chatou, France, 2017. Available online: http://www.opentelemac.org/ (accessed on 10 February 2026).
25. Mattic, O. *TELEMAC-3D User Manual*, version v8p0; EDF R&D-LNHE: Chatou, France, 2018.
26. Hervouet, J.M. *Hydrodynamics of Free Surface Flows: Modelling with the Finite Element Method*; John Wiley & Sons: Chichester, UK, 2007.
27. Erofeeva, S.Y.; Egbert, G.D. *OSU Tidal Prediction Software (OTPS)*; Oregon State University: Corvallis, Oregon, 2024. Available online: https://www.tpxo.net/otps (accessed on 10 February 2026).
28. Met Office Hadley Centre. *UKCP18 Simulated Impact of Mean Sea Level Change on Tidal Characteristics Around the UK*; Centre for Environmental Data Analysis: Didcot, UK, 2018.
29. Egbert, G.D.; Erofeeva, S.Y. Efficient inverse modeling of barotropic ocean tides. *J. Atmos. Ocean. Technol.* **2002**, *19*, 183–204. [CrossRef]
30. Morison, J.R.; Johnson, J.W.; Schaaf, S.A. The force exerted by surface waves on piles. *J. Pet. Technol.* **1950**, *2*, 149–154. [CrossRef]

31. Schlichting, H. *Boundary-Layer Theory*, 7th ed.; McGraw-Hill: New York, NY, USA, 1979.
32. Byrne, B.W.; Burd, H.J.; Zdravkovic, L.; Abadie, C.N.; Houlsby, G.T.; Jardine, R.J.; Martin, C.M.; McAdam, R.A.; Pacheco Andrade, M.; Pedro, A.M.; et al. PISA design methods for offshore wind turbine monopiles. In Proceedings of the Offshore Technology Conference (OTC), Houston, TX, USA, 6–9 May 2019.
33. Akhtar, N.; Geyer, B.; Schrum, C. Larger wind turbines as a solution to reduce environmental impacts. *Sci. Rep.* **2024**, *14*, 6608. [CrossRef] [PubMed]
34. Vermeer, L.J.; Sørensen, J.N.; Crespo, A. Wind Turbine Wake Aerodynamics. *Prog. Aerosp. Sci.* **2003**, *39*, 467–510. [CrossRef]
35. Wharton, S.; Julie, K.L.; Nikola, M. *Synergistic Effects of Turbine Wakes and Atmospheric Stability on Power Production at an Onshore Wind Farm*; LLNL-TR-524756; Lawrence Livermore National Laboratory: Livermore, CA, USA, 2012.
36. Peng, H.Y.; Lam, H.F.; Lee, C.F. Investigation into the Wake Aerodynamics of a Five-Straight-Bladed Vertical Axis Wind Turbine. *J. Wind. Eng. Ind. Aerodyn.* **2016**, *155*, 23–35. [CrossRef]
37. Platis, A.; Siedersleben, S.K.; Bange, J.; Lampert, A.; Bärfuss, K.; Hankers, R.; Cañadillas, B.; Foreman, R.; Schulz-Stellenfleth, J.; Djath, B.; et al. First in Situ Evidence of Wakes in the Far Field Behind Offshore Wind Farms. *Sci. Rep.* **2018**, *8*, 2163. [CrossRef] [PubMed]

Disclaimer/Publisher's Note: The statements, opinions and data contained in all publications are solely those of the individual author(s) and contributor(s) and not of MDPI and/or the editor(s). MDPI and/or the editor(s) disclaim responsibility for any injury to people or property resulting from any ideas, methods, instructions or products referred to in the content.